www.acsnano.org

Layer-Dependent Gas Sensing Mechanism of 2D Titanium Carbide (Ti₃C₂T_x) MXene Michael J. Loes, Saman Bagheri, and Alexander Sinitskii*

ACCESS

Metrics & More

Cite This: ACS Nano 2024, 18, 26251-26260

Article Recommendations

Read Online

Supporting Information

ABSTRACT: Monolayers of $Ti_3C_2T_x$ MXene and bilayer structures formed by partially overlapping monolayer flakes exhibit opposite sensing responses to a large scope of molecular analytes. When exposed to reducing analytes, monolayer MXene flakes show increased electrical conductivity, i.e., an n-type behavior, while bilayer structures become less conductive, exhibiting a p-type behavior. On the contrary, both monolayers and bilayers show unidirectional sensing responses with increased resistivity when exposed to oxidizing analytes. The sensing responses of $Ti_3C_2T_x$ monolayers and bilayers are dominated by entirely different mechanisms. The sensing behavior of MXene monolayers is dictated by the charge

Monolayer Overlapping
MXene flake MXene flakes

only adsorption, + intercalation, universal n-type sensing response resistance increase

transfer from adsorbed molecules and the response direction is consistent with the donor/acceptor properties of the analyte and the intrinsic n-type character of ${\rm Ti_3C_2T_x}$. In contrast, the bilayer MXene structures always show the same response regardless of the donor/acceptor character of the analyte, and the resistivity always increases because of the intercalation of molecules between the ${\rm Ti_3C_2T_x}$ layers. This study explains the sensing behavior of bulk MXene sensors based on multiflake assemblies, in which this intercalation mechanism results in universal increase in resistance that for many analytes is seemingly inconsistent with the n-type character of the material. By scaling MXene sensors down from multiflake to single-flake level, we disentangled the charge transfer and intercalation effects and unraveled their contributions. In particular, we show that the charge transfer has a much faster kinetics than the intercalation process. Finally, we demonstrate that the layer-dependent gas sensing properties of MXenes can be employed for the design of sensor devices with enhanced molecular recognition.

KEYWORDS: MXene, $T_{i3}C_2T_{xy}$ gas sensors, layer-dependent properties, intercalation, charge transfer

INTRODUCTION

Downloaded via SOUTH DAKOTA SCHOOL MINES & TECHLGY on September 30, 2024 at 00:42:42 (UTC). See https://pubs.acs.org/sharingguidelines for options on how to legitimately share published articles.

One of the notable attributes of two-dimensional (2D) materials is that their properties often strongly depend on the number of layers in 2D crystals. Examples of such layerdependent properties of 2D materials are very diverse, attracting fundamental interest and offering numerous technological applications. Many 2D materials, such as graphene, 1,2 transition metal dichalcogenides (TMDs), 3-5 phosphorene, 6,7 and others, have layer-dependent energy band gaps. For instance, monolayer graphene is a semimetal, while an AB-stacked bilayer graphene has a band gap that can be tuned by an electric field. 1,2 Many TMDs also have thickness-dependent photoluminescent properties-for instance, a monolayer MoS2 is a direct band gap semiconductor that can emit light, but a bilayer MoS2 has an indirect band gap and exhibits no photoluminescence.^{3,4} Some 2D materials were shown to have layer-dependent ferromagnetism^{8,9} and ferroelectricity. 10-12 Overall, these and other examples demonstrate that physical properties observed in a monolayer can often be significantly modified when a second identical

monolayer is stacked on top of it to form a bilayer structure, offering exciting opportunities for materials engineering.

In this paper, we demonstrate another example of layer-dependent properties of 2D materials. We studied materials from the family of MXenes – 2D transition metal carbides, nitrides, and carbonitrides with a general chemical formula of $M_{n+1}X_nT_x$, where M is a transition metal, X = C or N, n = 1-5, and T_x represents surface functional groups, such as -OH and -F. We show that the monolayers and bilayers of $Ti_3C_2T_x$, which is the most popular MXene material, 14,15 show opposite gas sensing responses to a large scope of molecular analytes. More specifically, when exposed to the same donor molecules, monolayer MXene flakes show increased electrical

Received: June 19, 2024 Revised: July 16, 2024 Accepted: July 23, 2024 Published: September 13, 2024





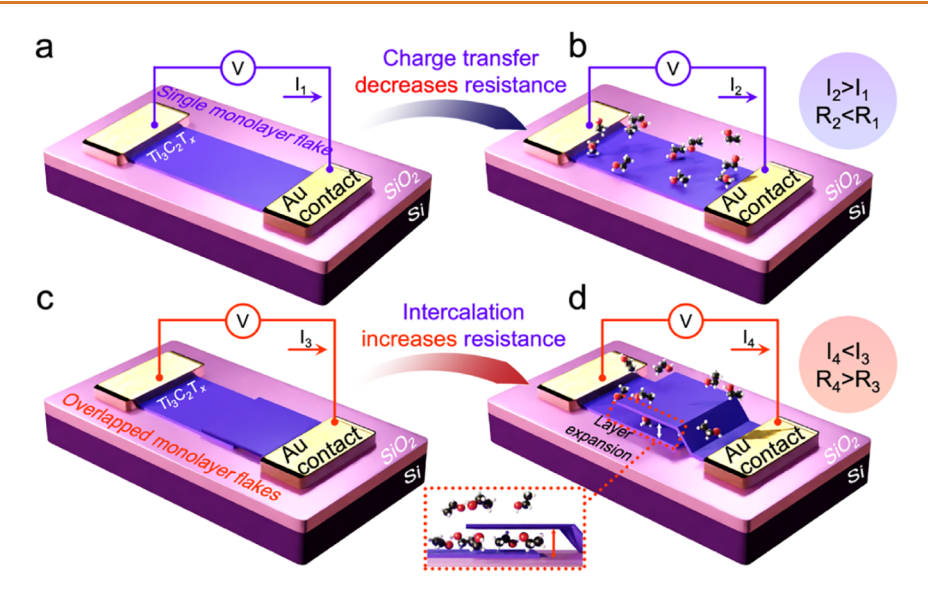


Figure 1. Schematic representation of the duality in the gas sensing mechanism for monolayer and bilayer MXene flakes. (a) Scheme of an electronic device based on monolayer $Ti_3C_2T_x$ flake. (b) Scheme of the same device as in (a) after the exposure to analyte molecules. If these are reducing molecules, the device current increases $(I_2 > I_1)$, i.e., the channel resistance decreases $(R_2 < R_1)$, as shown in the scheme. (c) Scheme of an electronic device based on two overlapping $Ti_3C_2T_x$ flakes that form a bilayer region in the middle of the channel. (d) Scheme of the same device as in (c) after the exposure to analyte molecules. Regardless of whether this is an oxidizing or reducing analyte, because of the intercalation of molecules between the layers (see the inset), the device current decreases $(I_4 < I_3)$, i.e., the channel resistance increases $(R_4 > R_3)$.

conductivity, while bilayer flakes become less conductive. Furthermore, we demonstrate that the sensing responses of $Ti_3C_2T_x$ monolayers and bilayers are dominated by *completely different mechanisms*.

The difference in the sensing responses of monolayer and bilayer MXene flakes that we discovered in this work is summarized in Figure 1. Figure 1a shows the scheme of an electronic device based on a monolayer flake of Ti₃C₂T_{xy} which was used to probe the gas sensing properties of this MXene. Electrical measurements of individual Ti₃C₂T_x flakes have previously shown their n-type transport behavior. 17-20 When an n-type channel is exposed to reducing molecules, such as alcohols, its resistance is expected to decrease (Figure 1b), while oxidizing molecules, such as NO2, should increase its resistance.²¹ Our studies that are disclosed in this paper confirm this behavior of an individual monolayer Ti₂C₂T_x flake. However, when bilayer Ti₃C₂T_x flakes (Figure 1c) are subjected to the same experiment, their gas sensing behavior is dominated by a different mechanism, which is based on the intercalation of the analyte molecules between the MXene layers (Figure 1d). Regardless of the donor or acceptor character of the analyte molecules, they all result in a larger channel resistance as the electrical contact between the layers becomes impaired due to the increased interlayer distance; see the inset in Figure 1d. Therefore, as illustrated by Figure 1, when exposed to the same reducing analyte, monolayer Ti₃C₂T_r flakes exhibit an n-type response with a decreased resistance while bilayer Ti₃C₂T_x flakes show an opposite, effectively p-type response with an increased resistance.

This study does not only facilitate engineering of sensing responses of MXene materials but also clarifies some of the previous results reported for MXene-based gas sensors. The field of MXene gas sensors has been very active in recent years, as evidenced by hundreds of experimental and theoretical publications as well as numerous topical reviews. These studies are motivated by many attractive characteristics of

MXene gas sensors, including their high sensitivity down to ppb levels, low noise, and tunability of properties enabled by the large compositional space of MXene materials that can be further expanded via possible functionalization and thermal treatment. 22,24,25 Importantly, all of the previous experimental studies of MXene sensors have been performed on multiflake assemblies, such as spin-coated or drop-cast films. Because of the complex interplay of charge transfer (Figure 1a,b) and intercalation effects (Figure 1c,d) in sensing experiments performed on multiflake MXene assemblies, the data interpretation could be complicated. In particular, it was difficult to reconcile the p-type sensing response (resistance increase) reported for gas sensors based on films of Ti₃C₂T_x flakes to reducing-type analytes^{24,26–29} with the n-type behavior observed in electrical measurements of individual $Ti_3C_2T_x$ flakes. ^{17–20} Some sensor studies even discussed $Ti_3C_2T_x$ as a p-type material.²⁸ It has been reported that the film thickness^{24,30,31} and intercalant history³¹⁻³⁹ may be important parameters when considering the design of MXene gas sensors, suggesting that the mechanism of electrical modulation in the film may be nontrivial compared to both semiconducting oxide gas sensors⁴⁰ and the current understanding of 2D gas sensors. 41 Various mechanistic solutions have been proposed to interpret the available data including a metallic conductor-type mechanism^{24,31,42} as well as an interflake swelling mechanism 32,37,41,43 that considers the contact resistance between neighboring flakes. In this study, by scaling MXene sensors down from multiflake to single-flake level, we disentangled the charge transfer and intercalation effects of analytes and studied them separately. We demonstrate the intrinsic n-type sensing response of individual Ti₃C₂T_r flakes and explain that the bulk assemblies of n-type MXene sheets can exhibit an effective p-type behavior because of intercalation of analyte molecules between flakes.

RESULTS AND DISCUSSION

In order to separately investigate the charge transfer and intercalation effects in gas sensing experiments, we fabricated two-terminal devices based on both monolayer ${\rm Ti_3C_2T_x}$ flakes and pairs of overlapping monolayer flakes, as schematically shown in Figure 1a,c, respectively. For the device fabrication, we prepared high-quality ${\rm Ti_3C_2T_x}$ MXene flakes following recent synthetic advances. Similar flakes were used in our recent study of the temperature-dependent electrical conductivity of ${\rm Ti_3C_2T_x}^{20}$ which provides detailed materials characterization of this MXene material by X-ray diffraction, X-ray photoelectron spectroscopy, and various microscopic techniques. The results of these analyses, which are discussed in detail in ref. 20, demonstrate the large size (>10 μ m in lateral dimensions), uniformity, and structural quality of ${\rm Ti_3C_2T_x}$ flakes prepared following the procedures reported in refs. 44,45.

While the detailed synthesis of these Ti₃C₂T_r flakes is described in ref. 20, here we briefly summarize several considerations that were taken into account for the preparation of a high-quality MXene material. First, we followed the optimized procedure for the synthesis of the precursor Ti₃AlC₂ MAX phase, which employed an excess of Al in the precursor mixture of TiC/Al/Ti compared to the stoichiometric ratio.⁴⁴ The resulting Ti₃AlC₂ MAX phase was previously shown to have fewer defects, which is beneficial for the synthesis of highquality MXene. 44 Second, we employed the minimally invasive layer delamination (MILD) method for the etching of Ti₃AlC₂ to produce Ti₃C₂T_x. The MILD method employs a mixture of LiF and HCl for the etching of Ti₃AlC₂, which is less aggressive than the concentrated HF, 46,47 and produces a MXene material of higher quality. 17,46 Finally, for the delamination of the etched MXene product into individual flakes, we followed the guidelines by Shekhirev et al., 45 avoiding any unnecessary agitation of a suspension to prevent tearing of large MXene sheets into smaller flakes. ¹⁷ Only a very mild shaking was used for the delamination of MXene particles in a suspension.⁴⁸

The resulting flakes that were deposited on a Si/SiO₂ substrate are shown in the optical photographs in Figure 2a,b. Since the MXene suspension was minimally disturbed, 45 many of the etched MXene particles were not fully delaminated, and the layers in such particles only slid relative to each other, forming multiple stacks of partially overlapping monolayers on a substrate. Such stacks of partially overlapping monolayers are very typical for the samples of MXenes produced by the soft delamination approach, 45 as illustrated by Figure 2a,b, where we show multiple unusually shaped flakes with a hole in the center, all of which originated from the same MAX phase particle. Figure 2c shows a representative transmission electron microscopy (TEM) image of an individual MXene monolayer. The flake was imaged on a lacey carbon TEM grid, which is seen as a dark weblike structure, and it was colored in blue for better visibility. In the case of partial oxidation of Ti₃C₂T_x flakes, microscopy analysis often reveals pinholes and elongated TiO2 particles, which are typically observed along the flake edges. 25,49 In our case, the imaged flake has a uniform surface and does not display pinholes or foreign particles, which suggests the high quality of the MXene material. The high quality of the MXene flake is further confirmed by the hexagonal selected-area electron diffraction (SAED) pattern (Figure 2d), which is consistent

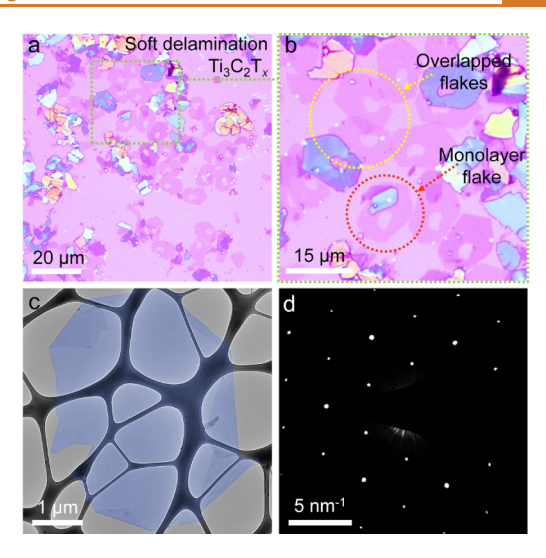


Figure 2. Microscopic characterization of MXene flakes produced by the soft delamination method. (a,b) Optical photographs of ${\rm Ti}_3{\rm C}_2{\rm T}_x$ flakes deposited on a ${\rm Si/SiO}_2$ substrate. (c) False-color TEM image of a monolayer MXene flake on a lacey carbon grid. The flake is colored in blue for clarity to distinguish it from the lacey carbon support. (d) SAED pattern of the monolayer ${\rm Ti}_3{\rm C}_2{\rm T}_x$ flake shown in panel (c).

with the structure of ${\rm Ti_3C_2T_x}$. The large size of MXene flakes produced by the soft delamination approach 45 as well as their tendency to form not only individual monolayers on substrates but also stacks of partially overlapping flakes (Figure 2a,b) makes such samples well suited for this study. We selected several pairs of partially overlapping MXene monolayers for the fabrication of bilayer ${\rm Ti_3C_2T_x}$ devices schematically shown in Figure 1c. We also fabricated several devices based on individual monolayer ${\rm Ti_3C_2T_x}$ flakes, as illustrated by the scheme in Figure 1a.

Representative devices based on monolayer and bilayer $Ti_3C_2T_x$ flakes are shown in Figure 3. One of the monolayer MXene devices fabricated in this study is shown in the optical microscopy image in Figure 3a. To confirm the monolayer thickness of this flake it was studied by atomic force microscopy (AFM), as shown in Figure 3b. The AFM height profile measured along the blue dashed line in Figure 3b shows a step height of about 2.4 nm, see Figure 3c, which is consistent with the previous AFM measurements of monolayer $Ti_3C_2T_x$ flakes on Si/SiO_2 substrates. 17,25,50 The increased height of $Ti_3C_2T_x$ flakes on Si/SiO_2 compared to the theoretical monolayer thickness of 0.98 nm 51,52 can be explained by the presence of surface adsorbates, such as water molecules. 17,25,50

Figure 3d shows an optical photograph of a representative device based on overlapping $\mathrm{Ti_3C_2T_x}$ monolayers. The gold electrodes were fabricated on the monolayer regions of two flakes, away from the overlapping bilayer region in between. In this device configuration, the channel current must pass from one flake to the overlapping region and then to the other flake, thus probing the effect of the interflake interface on the electronic and sensor properties of MXenes. AFM image of the channel of this device is shown in Figure 3e. The AFM height profile (Figure 3f) measured along the red dashed line in Figure 3e confirms the monolayer character of the individual flakes, as well as the larger thickness of the overlapping region

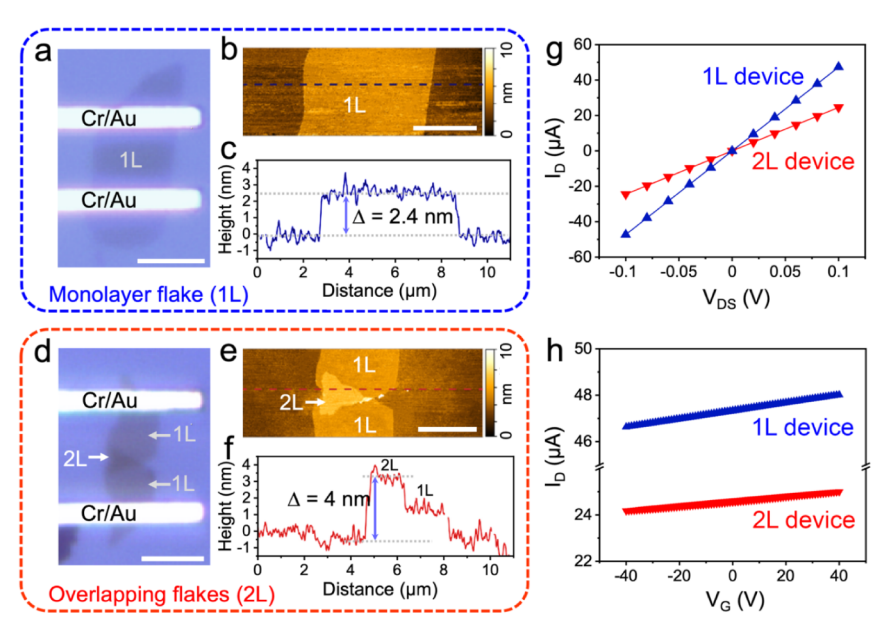


Figure 3. Electrical measurements and characterization of ${\rm Ti}_3{\rm C}_2{\rm T}_x$ devices. (a) Optical photograph of a device based on a monolayer MXene flake. Scale bar is 5 $\mu{\rm m}$. (b) AFM image of the central portion of the channel of the device shown in panel (a). Scale bar is 3 $\mu{\rm m}$. (c) AFM height profile measured across the monolayer MXene flake along the blue dashed line in panel (b). (d) Optical photograph of a device based on overlapping MXene flakes. Scale bar is 5 $\mu{\rm m}$. Monolayer (1L) and bilayer (2L) regions of the device channel are marked by the arrows. (e) AFM image of the central portion of the channel of the device shown in panel (d). Scale bar is 3 $\mu{\rm m}$. (f) AFM height profile measured along the red dashed line in panel (e) showing the height steps corresponding to the monolayer and bilayer regions of the device channel. (g) $I_{\rm D}$ - $V_{\rm DS}$ dependences for the monolayer (1L, panel (a)) and bilayer (2L, panel (d)) MXene devices. (h) $I_{\rm D}$ - $V_{\rm G}$ dependences for the monolayer (1L, panel (d)) MXene devices. The measurements were performed at $V_{\rm DS}=0.1~{\rm V}$.

of about 4 nm. This thickness is consistent with the results of previous AFM measurements of bilayer $Ti_3C_2T_x$ flakes. ^{17,19}

The electrical measurements of the MXene devices were performed using the lithographic gold contacts as source (S) and drain (D) electrodes and the p-doped silicon substrate as the gate (G) electrode. The silicon substrate was covered with a 90 nm-thick layer of SiO₂, which served as a gate dielectric. We measured both monolayer and bilayer devices and compared their room-temperature dependences of the drain current (I_D) on the drain-source voltage (V_{DS}) at the gate voltage $V_{\rm G}$ = 0, see Figure 3g. Interestingly, we did not observe a significant difference in the conductivities of monolayer and bilayer devices. The device based on overlapping Ti₂C₂T_w flakes shows a linear I_D - V_{DS} curve, similar to the monolayer device (Figure 3g). While the in-plane current in the bilayer device (Figure 3d) was smaller than in the monolayer device (Figure 3a) by a factor of about 2, the bilayer device had a considerably larger source-drain distance (7.32 μ m versus 4.5 μ m for the monolayer device), so that when the geometrical parameters of the devices were taken into account, both devices exhibited comparable electrical conductivities of about 4000 S/cm, which is similar to our previous reports for monolayer ${\rm Ti_3C_2T_x}$ flakes. 17,19,20,45 This result suggests that the electrical contacts between the Ti₃C₂T_x flakes are very good and do not cause a precipitous drop in electrical conductivity compared to the single-flake devices. 17-20 Overall, the topic of contact resistances between flakes is of significant importance for many applications of MXenes, such as conductive thin films⁵³ and energy storage,⁵¹ and thus requires a separate investigation. Yet, the good electrical contact between the flakes suggested by the data in Figure 3g is consistent with the fact that the reported electrical conductivities of Ti₃C₂T_x films consisting of multiple overlapping flakes 44,51 were often comparable to the results of electrical measurements on individual ${\rm Ti_3C_2T_x}$ flakes, 17,19,20,45 which would not be possible if the interflake contact resistances were high.

Figure 3h shows I_D - V_G dependences for both monolayer and bilayer MXene devices. Both dependences are linear and have a positive slope, which is consistent with the previously reported n-type behavior of ${\rm Ti}_3 C_2 {\rm T_x}^{17-20,45}$ While the MXene devices tested in this study showed a larger modulation of the I_D in response to $V_{\rm G}$ compared to our previous reports, 17,19,20 this is primarily due to the fact that here we used a thinner gate dielectric (the thickness of SiO₂ was 90 nm as opposed to the usual 300 nm). The calculated electron mobilities for the tested devices were in the range of 3-5 cm² V⁻¹ s⁻¹, which is consistent with our previous measurements of Ti₃C₂T_x flakes. 17,19,20 The n-type behavior of both monolayer and bilayer structures (Figure 3h) is seemingly inconsistent with the previously reported p-type sensing response of $Ti_3C_2T_{r}$ when reducing analytes, such as low-molecular-weight alcohols, acetone, ammonia and others, were shown to cause an increase in resistance when adsorbed on multiflake Ti₃C₂T_x sensors. 24-27,54,55 Thus, we performed gas sensing experiments on the fabricated devices (Figure 3) to elucidate how reducing analytes could induce a seemingly p-type response in an n-type $Ti_3C_2T_{xy}$ if the MXene material was tested in a bulk form.

For the sensing measurements, the devices were wire bonded to a chip carrier, as shown in Figure S1; additional information on the chip carrier and the measurement setup can be found in the Experimental section. Figure 4a shows the sensing responses to a reducing (ethanol) and oxidizing (NO₂) analyte for both types of devices. Here, the response is defined as $\frac{(R_a - R_b)}{R_b} \times 100\%$, where R_a and R_b are the resistances of the device under analyte and baseline (nitrogen) atmospheres, respectively. We first discuss the behavior of monolayer

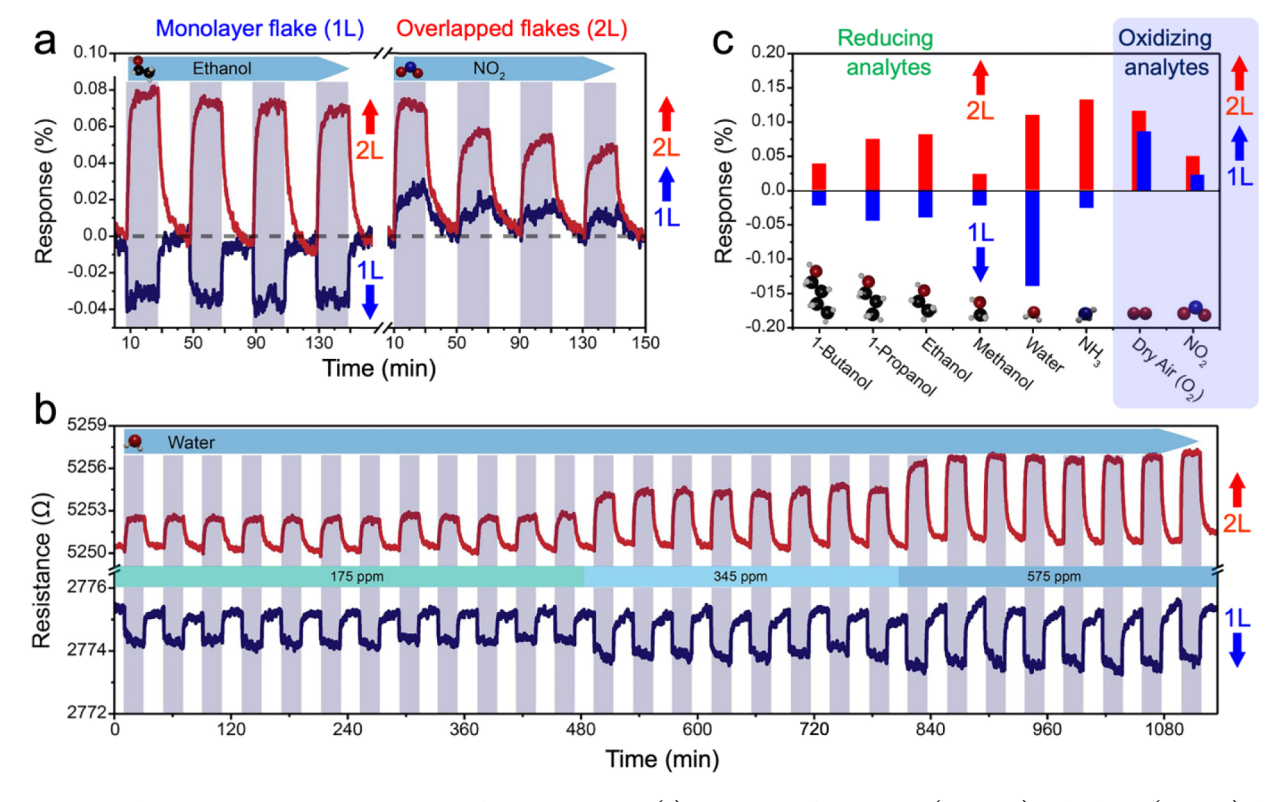


Figure 4. Layer-dependent gas sensing mechanism of $Ti_3C_2T_x$ MXene. (a) Responses of monolayer (1L; blue) and bilayer (2L; red) devices to a reducing gas (ethanol, 1460 ppm) and an oxidizing gas (NO₂, 1 ppm) showing qualitatively different responses. (b) Reproducibility of the opposite responses of monolayer (1L; blue) and bilayer (2L; red) devices to water at different concentrations. In panels (a) and (b), gray vertical stripes correspond to analyte dosing while white vertical stripes correspond to N₂ purging. (c) Histogram of averaged responses of several monolayer (1L; blue) and bilayer (2L; red) devices to selected oxidizing (1 atm dry air (O₂); NO₂ (1 ppm)) and reducing analytes (1-butanol (165 ppm); 1-propanol (585 ppm); ethanol (1460 ppm); methanol (7390 ppm); H₂O (1375 ppm); NH₃ (10 ppm)). These molecules had different concentrations (see the Experimental section for details) and therefore the histogram presents a qualitative comparison between the groups of analytes with donor and acceptor properties rather than a quantitative comparison between specific analytes. It should also be noted that the responses of devices based on overlapping flakes to various analytes should depend on their geometrical parameters, such as the ratio of 1L and 2L regions. While this histogram qualitatively shows the difference in the behavior of 1L and 2L devices, the magnitudes of the red bars may change for a different set of 2L devices.

Ti₃C₂T_x devices. Figure 4a shows that unlike the previous reports on bulk $Ti_3C_2T_x$ sensors, 24,26,27 which exhibited increased resistance (i.e., a p-type response) upon exposure to reducing gases, such as ethanol, here the monolayer devices show the expected n-type sensing response to ethanol with decreased resistance. Furthermore, when monolayer Ti₃C₂T_r devices are exposed to an oxidizing gas, such as NO2, they also show the expected n-type sensing response, as the resistance increases. Thus, by performing gas sensing experiments on individual MXene monolayers, we demonstrate the intrinsic ntype sensing behavior of Ti₃C₂T_x. In fact, we show that monolayer Ti₃C₂T_x behaves in the same way as other monolayer 2D materials with sensing responses induced by the charge transfer from molecules with donor or acceptor character. For example, monolayer MoS2, which is also an ntype material, similarly shows decreased resistance in response to reducing gases and increased resistance in response to oxidizing gases.56

The fact that ${\rm Ti}_3{\rm C}_2{\rm T}_x$ monolayers with metallic conductivity show a sensing response through a charge transfer mechanism is related to their extreme thinness. A bulk piece of a metal contains too many free electrons for charge transfer from adsorbed molecules to make a noticeable change in electrical conductivity. However, a ${\rm Ti}_3{\rm C}_2$ monolayer without the surface groups has a thickness of only about 1 nm. 51,52

Therefore, given that $\mathrm{Ti_3C_2T_x}$ has a carrier concentration of about 10^{22} cm⁻³, as shown in several studies, 18,20,57 and assuming that an adsorbed analyte molecule has a footprint of about 1 nm² (all the tested molecules in this study were actually smaller), the corresponding volume of a MXene monolayer (1 nm³) contains only about 10 electrons; see Figure S2. Given that this number is relatively small, an adsorbed electron-donating molecule can produce a noticeable increase in electrical conductivity, in accord with the n-type sensing behavior. The extreme thinness of MXene monolayers is also the reason why they can be gated in field-effect measurements (Figure 3h) showing n-type behavior, $^{17-20}$ despite the metallic nature of $\mathrm{Ti_3C_2T_x}$.

The sensing behavior of the devices radically changes with the addition of a single MXene monolayer, creating an overlapping structure. Regardless of the donor/acceptor character of molecules, the resistance of bilayer devices always *increases* upon the exposure to the analyte, as shown in Figure 4a for both ethanol and NO₂. These results are consistent with the previously reported behavior of bulk Ti₃C₂T_x sensors based on films of overlapping flakes. ^{24,26,27} Since a MXene monolayer is shown to exhibit an n-type behavior, the change in the sensing response when two such monolayers are stacked in a bilayer structure should be related to the emergence of an interlayer spacing between the overlapping flakes. Given that

various molecular species are known to intercalate between stacked MXene flakes, 33,58 it is most plausible that such an intercalation process is responsible for the universal increase in resistance of bilayer devices in response to all analytes. As schematically shown in the inset in Figure 1d, the molecular intercalation between the flakes increases the interlayer distance and thus the interflake contact resistance regardless of the donor or acceptor character of the analyte. While for bilayer devices there should be a competition between the charge transfer and intercalation mechanisms, the fact that for reducing analytes the sensing response completely reverts compared to monolayer devices suggests that the intercalation mechanism is dominant. Correspondingly, in the previously reported bulk MXene sensors^{24–27} based on overlapping flakes there were multiple interlayer spaces for molecular intercalation, 43 and this intercalation mechanism (Figure 1d) was responsible for the observed universal resistance increase, masking the charge transfer interactions between the analytes and MXene materials.

While we first illustrated the duality in the gas sensing mechanism for monolayer and bilayer MXene flakes (Figure 1) using a pair of ethanol, a reducing analyte, and NO2, an oxidizing analyte (Figure 4a), the same behavior was observed for a variety of other molecular species. For example, Figure 4b shows the responses of monolayer and bilayer devices to water, again demonstrating their opposite behaviors. Similar to ethanol, exposure of MXene sensors to water molecules decreases the resistance of monolayer devices because of the charge transfer (Figure 1a,b) and increases the resistance of bilayer devices because of the molecular intercalation between the flakes (Figure 1c,d). It should be noted that the intercalation of both ethanol and water molecules between the Ti₃C₂T_x layers is facilitated by the hydrogen bonding interactions between the analyte and the MXene surface functional groups, and the resistance of the channel increases as a result of this separation. We also demonstrate that these opposite responses are very reproducible and observed at different analyte concentrations (Figure 4b).

The responses of the tested devices (four pairs of overlapping flakes and four monolayer flakes) to multiple analytes are summarized in Figure 4c showing that the described behavior (Figure 1) is reproducible. The response of devices with overlapping flakes is always positive, with an increase in resistance on exposure to all analytes. In contrast, the monolayer devices show negative response to five reducing-type vapors (1-butanol, 1-propanol, ethanol, methanol, water), but positive response to two oxidizing-type vapors (NO₂ and O₂). The pristine ${\rm Ti}_3{\rm C}_2{\rm T}_x$ sensor should have an affinity for H₂O according to both mechanisms because of the hydrophilicity of the surface functional groups facilitating both adsorption (charge transfer) and intercalation.

Further evidence for the dual sensing mechanism is given by Figure 5. Figure 5a shows multiple sensing cycles of representative monolayer and bilayer ${\rm Ti_3C_2T_x}$ devices to ethanol. As ethanol is a reducing gas, the devices show opposite sensing behaviors. Both responses are shown on the same resistance scale, and the response magnitude for the bilayer device is visibly larger than for the monolayer device, again demonstrating that the molecular intercalation is the dominant mechanism. Furthermore, response time to ethanol is more than an order of magnitude faster for the monolayer device compared to the overlapping flakes (Figure 5b,c). Since the response of the monolayer is based solely on adsorption

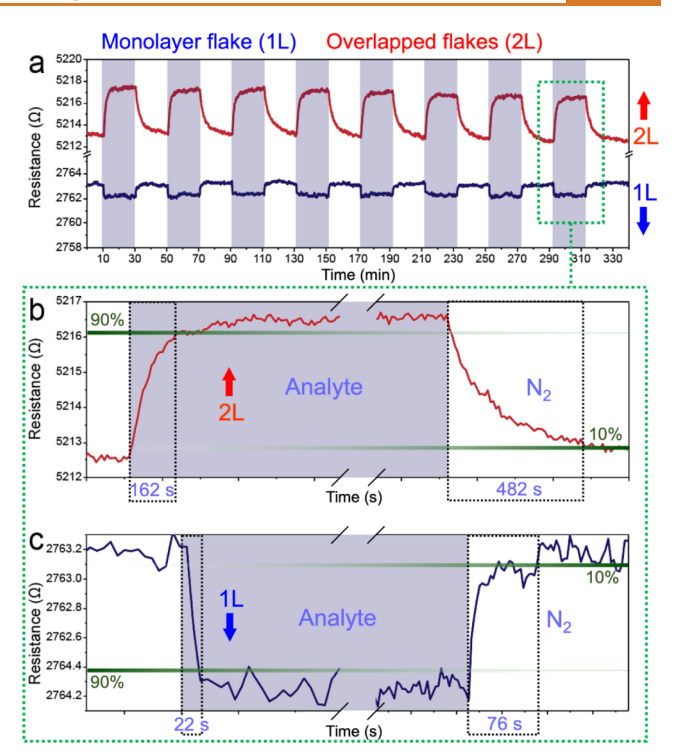


Figure 5. Kinetics of responses of monolayer and bilayer $Ti_3C_2T_x$ devices to ethanol. (a) Reproducibility of the opposite responses of monolayer (1L; blue) and bilayer (2L; red) devices to ethanol at a concentration of 1460 ppm. Both responses are shown on the same resistance scale. Gray vertical stripes correspond to analyte dosing while white vertical stripes correspond to N_2 purging. (b) One of the sensing cycles from panel (a) for a bilayer device showing relatively long response (162 s) and recovery (482 s) times, which were measured at 90% of the resistance change. (c) One of the sensing cycles from panel (a) for a monolayer device showing much shorter response (22 s) and recovery (76 s) times compared to a bilayer device.

and charge transfer to the available surface, the dynamic equilibrium is established quickly at a given concentration. In contrast, the response of the overlapping flakes is diffusion limited, and therefore the device responds much slower as molecules require time to intercalate between the layers. The same relationship is seen for the desorption/deintercalation, however the time is increased in both cases due to the spontaneous nature of ethanol adsorption on the MXene sensing substrate (i.e., negative adsorption energy). ⁵⁹

The difference in the kinetics of the two competing sensing mechanisms is further illustrated by Figure S3. As we discussed above, the intercalation mechanism has a stronger effect on the resistance of a bilayer device but is also much slower than the charge transfer mechanism. As a result, for certain bilayer devices exposed to reducing analytes it is possible to observe that the resistance would first decrease due to the charge transfer effect in the top surface of the channel, but then when sufficient time passes for the molecules to intercalate between the flakes, the resistance would increase (Figure S3). Correspondingly, a purging of such devices with nitrogen would quickly desorb analytes from the top surface, causing a temporary increase in resistance, but then with the progression of a slower deintercalation process the resistance would decrease. For most bilayer devices tested in this study, the intercalation mechanism dominated the sensing response, and these signatures of the charge transfer mechanism were not

observed. However, the 2L device shown in Figure S3 clearly exhibits these spikes in resistance in the beginning of the exposure and purging cycles, providing more evidence for the competition of two sensing mechanisms. One of the factors affecting the presence of these spikes could be the ratio of 1L and 2L areas in bilayer devices. In this light, a possible future study may focus on quantifying the contributions of each mechanism based on the areas of both the exposed surfaces and the interface as well as the interflake separation distance.

The fact that a MXene material can show different responses to the same analyte depending on the number of layers in a sensor offers exciting opportunities for engineering discriminative sensing devices. A possible simple and practical sensor architecture is presented in Figure 6a, which shows a device

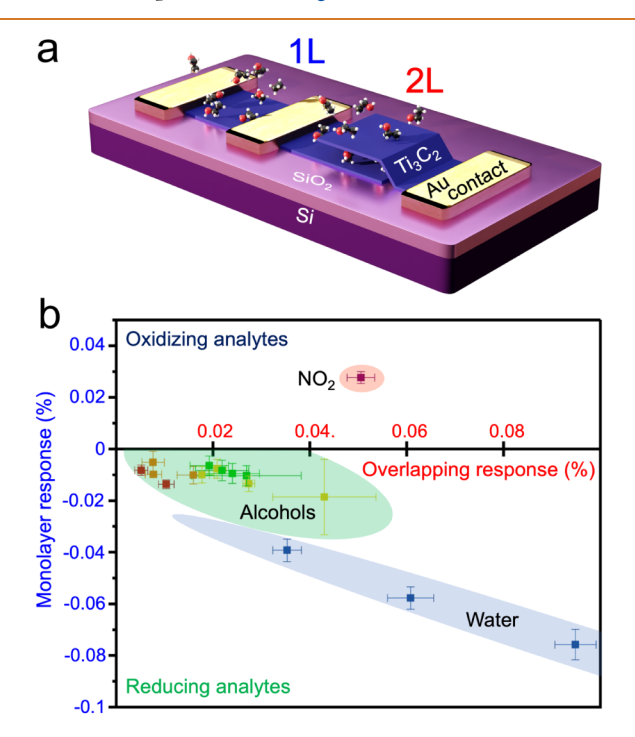


Figure 6. A concept of a compact MXene-based device for discriminative gas sensing. (a) Scheme of a proposed selective MXene sensor device comprising a monolayer (1L) and a bilayer (2L) segment. (b) Two-dimensional response plot showing easy segregation of analytes. The alcohols are labeled as follows: red = 1-butanol (60-180 ppm); orange = 1-propanol (175-875 ppm); yellow = ethanol (228-2280 ppm); green = methanol (683-6830 ppm). Other concentrations include 170-575 ppm for water and 1 ppm for NO₂. The data for dry air and 2-4 ppm of NO₂ are in the same quadrant of oxidizing gases but outside the scale.

composed of two sensing channels—one that collects the surface response, and another that monitors an area of overlapping MXene flakes. The advantage of such sensor is that the signals in the 1L and 2L channels are induced by entirely different mechanisms, charge transfer and intercalation, respectively. In turn, these mechanisms depend on different parameters of the analyte molecules, i.e., the charge transfer properties depend on the molecular structure and atomic electronegativities, while important parameters for the intercalation include the size of molecules and their affinity to MXene sheets. In other words, it would be unlikely for two different molecules to produce identical both charge transfer effect on the monolayer channel and intercalation effect on the bilayer channel. This idea is illustrated by Figure 4c, which

shows that all eight analytes have different $\alpha = Resp.(2L)/Resp.$ (1L) ratios, where Resp.(1L) and Resp.(2L) are the sensing responses of the monolayer and bilayer MXene devices when exposed to an analyte at the same concentration (both Resp. (1L) and Resp.(2L) are concentration dependent). For oxidizing molecules $\alpha > 0$, for reducing molecules $\alpha < 0$, and within each group of analytes in Figure 4c all α values are visibly different.

Another way to visualize the selectivity of a two-channel MXene sensor (Figure 6a) is to construct a 2D plot of the monolayer-type response versus overlapping-type response space, as shown in Figure 6b. Each data point in this plot represents a Cartesian coordinate pair of (Resp. (2L), Resp. (1L)) when the 1L and 2L channels are exposed to the same analyte at a certain concentration. As different molecules are characterized by different α values, the analytes visibly segregate in different areas of the plot, enabling their recognition. For example, it is possible that water and ethanol taken at certain concentrations would produce comparable intercalation effects on the bilayer (x-axis) channel, resulting in sensing responses of about 0.04%. In this case, these analytes will be discriminated by the monolayer (y-axis) channel, which would show responses of about -0.02% for ethanol and about -0.04% for water. While a more comprehensive screening of additional analytes and concentrations will reveal the selectivity limits for this two-channel device, the plot in Figure 6b, which demonstrates a larger data set than that displayed in Figure 4c, already shows the promise of this 2D representation approach for discriminative gas sensing. One notable advantage of this representation is the visibility of the concentration dependence. Within the subset of data points corresponding to each analyte (see the color information in the description of Figure 6b), the response to lower concentrations is closer to the origin, while the response to higher concentration is further. The slope of this curve for each analyte is related to the parameter α . The dependences are mostly linear across the tested concentration ranges, although this linearity is not expected to continue as the device becomes saturated with high analyte concentrations.

CONCLUSIONS

In summary, we have reported layer-dependent gas sensing properties of Ti₃C₂T_x MXene. We have also demonstrated the intrinsic n-type response from gas sensors based on pristine Ti₃C₂T_x by fabricating devices at the monolayer limit and investigating their response to various oxidizing and reducing gases. We confirmed that monolayer $Ti_3C_2T_x$ responds to the adsorbed gas based on the accepted charge transfer mechanism of 2D material gas sensors. We also expanded on the current understanding to include the effect of layer separation in bilayer and multilayer MXene structures as a competing mechanism of response. The demonstrated approach of comparing the sensing responses of individual and overlapping flakes can be applied to many different MXene systems beyond the conventional Ti₃C₂T_x, including other MXene compositions 13-16,31,37 as well as MXenes with different surface terminations, ^{39,59} intercalants, ^{32,39} and various composite structures. 25,28,29,49 Since the intercalation of the tested analyte molecules between layers is facilitated by the abundance of hydrophilic surface terminations on MXene, the effect of flake separation is emphasized, but similar processes should be entertained when discussing the sensing mechanism of 2D film-based chemiresistive gas sensors in general. Of particular

relevance are similarly terminated materials like graphene oxide and reduced graphene oxide ^{60,61} and sensors based on a drop-cast or film morphology where electron transport between homojunctions is necessary to form a closed circuit. For an n-type conductor, the competition between these mechanisms has been demonstrated in this work on adsorption to reducing gas. Interestingly, for a true p-type conductor, it should be expected that these mechanisms would compound each other, and the resulting response would be the sum of both effects.

This work not only clarifies the sensing mechanism of MXene gas sensors, but also has far-reaching implications for the application of 2D materials, particularly MXenes, for gas sensing. We demonstrate that the layer-dependent gas sensing properties of MXenes can be employed for the design of sensor devices with enhanced molecular recognition. In particular, we show that monolayer and bilayer/multilayer MXene devices can be combined into a two-channel sensing structure, for which a 2D representation of the channel responses enables a very straightforward analyte discrimination. We expect that the results of this work will facilitate the directed design of functional devices and enable interesting device architectures that take advantage of the layer-dependent gas sensing mechanism in MXenes and possibly other 2D materials.

EXPERIMENTAL SECTION

Device Fabrication and Electrical Measurements. Ti₃AlC₂ MAX phase and $Ti_3C_2T_x$ MXene were synthesized according to our previous report,²⁰ which also contains details of the structural and spectroscopic characterization of both materials. The synthesis resulted in a dark green aqueous solution of MXene flakes that was used for the device fabrication. The flakes were drop-cast onto a heavily p-doped Si substrate covered with a 90 nm-thick layer of SiO₂ (Wafer University) and some of them were selected for the device fabrication using optical microscopy. A Zeiss Supra 40 field-emission scanning electron microscope and a Raith pattern generator were used for electron beam lithography to pattern electrodes on MXene flakes. Metal contacts comprising layers of Cr (5 nm; deposition rate of 0.2 Å/s) and Au (50 nm; deposition rate of 0.8 Å/s) were deposited with an AJA International ATC-2000F plasma sputtering system using a DC power source. The I_D - V_{DS} and I_D - V_G characteristics of the freshly prepared MXene devices were measured in a Lake Shore TTPX cryogenic probe station at a base pressure of about 2×10^{-6} Torr. After the evacuation, the devices were stored in vacuum for at least 2 days before the measurements to minimize the effect of surface adsorbates on the electronic characteristics.

After the $I_{\rm D}$ - $V_{\rm DS}$ and $I_{\rm D}$ - $V_{\rm G}$ characterization, the devices were bonded to a sensor chip carrier (Figure S1), that was similar to those used in our previous studies of sensing and electronic properties of 2D materials. ^{25,61,62} The wire bonding was performed using a West Bond 7400E manual wedge bonder and 0.001" Au wire (99.99% Au, SPM) without substrate heating to preserve the quality of ${\rm Ti}_3{\rm C}_2{\rm T}_x$. After the wire bonding, the electrical conductivity of the MXene devices was checked to confirm that they did not degrade.

Sensor Measurements. Sensor experiments were performed in a home-built sensor test system that is described in detail in our previous works. The system allows for the generation of ppm analyte vapors in a carrier gas by evaporation from diffusion vials and dilution with N_2 . We used diffusion vials for dosing most of the analytes used in this study (1-butanol, 1-propanol, ethanol, methanol, and water). The concentration of these vapors in the mixture was determined gravimetrically after each experiment by performing mass measurements of the remaining liquids to an accuracy of 0.1 mg. NO_2 (1 ppm in N_2) and NH_3 (10 ppm in N_2) were dosed from commercial calibration gas cylinders (Airgas). Dry air (N_2/O_2 mixture) was dosed from a compressed air cylinder (Matheson). Continuous flow through the sensor test system was governed by three MKS thermal mass flow controllers calibrated to N_2 with various full range scales (50–500

sccm). A Keithley 2401 source meter was used for both applying an electrical bias and measuring the resulting current flow through each two-terminal device, and a Keithley 7001 switch system enabled the measurement of all devices in parallel. The system was controlled by a LabVIEW program that was written specifically for this experiment. The sensor measurements were taken continuously for 2 weeks following the initial device fabrication, and the ${\rm Ti}_3{\rm C}_2{\rm T}_x$ devices were kept under inert ${\rm N}_2$ atmosphere through the entire experiment to minimize unwanted oxidation of the MXene flakes. Before the measurements, the chip was purged with nitrogen for 2 days to ensure desorption of atmospheric oxygen and water adsorbates from the MXene surface (Figure S4).

Materials Characterization. TEM and SAED of MXene flakes were performed using a FEI Tecnai Osiris scanning transmission electron microscope equipped with a HAADF detector and a X-FEG high brightness Schottky field emission gun. The accelerating voltage was 200 kV. SEM was performed using a Zeiss Supra 40 field-emission scanning electron microscope at the accelerating voltage of 5 kV. AFM was performed using a Bruker Dimension Icon atomic force microscope.

ASSOCIATED CONTENT

Supporting Information

The Supporting Information is available free of charge at https://pubs.acs.org/doi/10.1021/acsnano.4c08225.

Optical photograph of the $\mathrm{Si/SiO_2}$ substrate with MXene devices (Figure S1); scheme of the n-type sensing response by a monolayer of metallic $\mathrm{Ti_3C_2T_x}$ (Figure S2); illustration of competing charge transfer and intercalation gas sensing mechanisms in a device based on overlapping MXene flakes (Figure S3); resistance changes of two devices based on monolayer and bilayer $\mathrm{Ti_3C_2T_x}$ flakes while pumping from atmosphere to vacuum (Figure S4) (PDF)

AUTHOR INFORMATION

Corresponding Author

Alexander Sinitskii — Department of Chemistry and Nebraska Center for Materials and Nanoscience, University of Nebraska-Lincoln, Lincoln, Nebraska 68588, United States; orcid.org/0000-0002-8688-3451; Email: sinitskii@ unl.edu

Authors

Michael J. Loes — Department of Chemistry and Nebraska Center for Materials and Nanoscience, University of Nebraska-Lincoln, Lincoln, Nebraska 68588, United States Saman Bagheri — Department of Chemistry and Nebraska Center for Materials and Nanoscience, University of Nebraska-Lincoln, Lincoln, Nebraska 68588, United States; orcid.org/0000-0002-4206-3021

Complete contact information is available at: https://pubs.acs.org/10.1021/acsnano.4c08225

Notes

The authors declare no competing financial interest.

ACKNOWLEDGMENTS

The work was supported by the National Science Foundation through awards OIA-2044049 (MXene synthesis) and OSI-2329159 (device fabrication, electrical and sensor measurements). Some experiments were performed using the instrumentation at the UNL instrumentation facilities supported by the National Science Foundation (award

ECCS-2025298), the Nebraska Research Initiative, and the Nebraska Center for Energy Sciences Research.

REFERENCES

- (1) Min, H.; Sahu, B.; Banerjee, S. K.; MacDonald, A. H. *Ab initio* theory of gate induced gaps in graphene bilayers. *Phys. Rev. B* **2007**, 75, 155115.
- (2) Zhang, Y.; Tang, T.-T.; Girit, C.; Hao, Z.; Martin, M. C.; Zettl, A.; Crommie, M. F.; Shen, Y. R.; Wang, F. Direct observation of a widely tunable bandgap in bilayer graphene. *Nature* **2009**, *459*, 820–823.
- (3) Mak, K.; Lee, C.; Hone, J.; Shan, J.; Heinz, T. Atomically Thin MoS₂: A New Direct-Gap Semiconductor. *Phys. Rev. Lett.* **2010**, *105*, 136805.
- (4) Splendiani, A.; Sun, L.; Zhang, Y.; Li, T.; Kim, J.; Chim, C.-Y.; Galli, G.; Wang, F. Emerging Photoluminescence in Monolayer MoS₂. *Nano Lett.* **2010**, *10*, 1271–1275.
- (5) Li, J.; Kolekar, S.; Ghorbani-Asl, M.; Lehnert, T.; Biskupek, J.; Kaiser, U.; Krasheninnikov, A. V.; Batzill, M. Layer-Dependent Band Gaps of Platinum Dichalcogenides. *ACS Nano* **2021**, *15*, 13249–13259.
- (6) Liu, H.; Neal, A. T.; Zhu, Z.; Luo, Z.; Xu, X.; Tománek, D.; Ye, P. D. Phosphorene: An Unexplored 2D Semiconductor with a High Hole Mobility. *ACS Nano* **2014**, *8*, 4033–4041.
- (7) Tran, V.; Soklaski, R.; Liang, Y.; Yang, L. Layer-controlled band gap and anisotropic excitons in few-layer black phosphorus. *Phys. Rev. B* **2014**, *89*, 235319.
- (8) Huang, B.; Clark, G.; Navarro-Moratalla, E.; Klein, D. R.; Cheng, R.; Seyler, K. L.; Zhong, D.; Schmidgall, E.; McGuire, M. A.; Cobden, D. H.; Yao, W.; Xiao, D.; Jarillo-Herrero, P.; Xu, X. Layer-dependent ferromagnetism in a van der Waals crystal down to the monolayer limit. *Nature* **2017**, *546*, 270–273.
- (9) Son, J.; Son, S.; Park, P.; Kim, M.; Tao, Z.; Oh, J.; Lee, T.; Lee, S.; Kim, J.; Zhang, K.; Cho, K.; Kamiyama, T.; Lee, J. H.; Mak, K. F.; Shan, J.; Kim, M.; Park, J.-G.; Lee, J. Air-Stable and Layer-Dependent Ferromagnetism in Atomically Thin van der Waals CrPS₄. ACS Nano **2021**, *15*, 16904–16912.
- (10) Fei, R.; Kang, W.; Yang, L. Ferroelectricity and Phase Transitions in Monolayer Group-IV Monochalcogenides. *Phys. Rev. Lett.* **2016**, *117*, 097601.
- (11) Cui, C.; Hu, W.-J.; Yan, X.; Addiego, C.; Gao, W.; Wang, Y.; Wang, Z.; Li, L.; Cheng, Y.; Li, P.; Zhang, X.; Alshareef, H. N.; Wu, T.; Zhu, W.; Pan, X.; Li, L.-J. Intercorrelated In-Plane and Out-of-Plane Ferroelectricity in Ultrathin Two-Dimensional Layered Semiconductor In₂Se₃. *Nano Lett.* **2018**, *18*, 1253–1258.
- (12) Yasuda, K.; Wang, X.; Watanabe, K.; Taniguchi, T.; Jarillo-Herrero, P. Stacking-engineered ferroelectricity in bilayer boron nitride. *Science* **2021**, *372*, 1458–1462.
- (13) Naguib, M.; Mochalin, V. N.; Barsoum, M. W.; Gogotsi, Y. 25th Anniversary Article: MXenes: A New Family of Two-Dimensional Materials. *Adv. Mater.* **2014**, *26*, 992–1005.
- (14) Gogotsi, Y.; Anasori, B. The Rise of MXenes. ACS Nano 2019, 13, 8491-8494.
- (15) Anasori, B.; Gogotsi, Y. 2D Metal Carbides and Nitrides (MXenes): Structure, Properties and Applications; Springer International Publishing, 2019.
- (16) Vahidmohammadi, A.; Rosen, J.; Gogotsi, Y. The world of two-dimensional carbides and nitrides (MXenes). *Science* **2021**, *372*, No. eabf1581.
- (17) Lipatov, A.; Alhabeb, M.; Lukatskaya, M. R.; Boson, A.; Gogotsi, Y.; Sinitskii, A. Effect of Synthesis on Quality, Electronic Properties and Environmental Stability of Individual Monolayer Ti₃C₂ MXene Flakes. *Adv. Electron. Mater.* **2016**, *2*, 1600255.
- (18) Miranda, A.; Halim, J.; Barsoum, M. W.; Lorke, A. Electronic properties of freestanding $Ti_3C_2T_x$ MXene monolayers. *Appl. Phys. Lett.* **2016**, *108*, 033102.
- (19) Lipatov, A.; Goad, A.; Loes, M. J.; Vorobeva, N. S.; Abourahma, J.; Gogotsi, Y.; Sinitskii, A. High electrical conductivity and

- breakdown current density of individual monolayer $Ti_3C_2T_x$ MXene flakes. *Matter* **2021**, *4*, 1413–1427.
- (20) Lipatov, A.; Bagheri, S.; Sinitskii, A. Metallic Conductivity of $Ti_3C_2T_x$ MXene Confirmed by Temperature-Dependent Electrical Measurements. *ACS Mater. Lett.* **2024**, *6*, 298–307.
- (21) Goel, N.; Kunal, K.; Kushwaha, A.; Kumar, M. Metal oxide semiconductors for gas sensing. *Eng. Rep.* **2023**, *5*, No. e12604.
- (22) Bhardwaj, R.; Hazra, A. MXene-based gas sensors. J. Mater. Chem. C 2021, 9, 15735-15754.
- (23) Mehdi Aghaei, S.; Aasi, A.; Panchapakesan, B. Experimental and Theoretical Advances in MXene-Based Gas Sensors. *ACS Omega* **2021**, *6*, 2450–2461.
- (24) Kim, S. J.; Koh, H.-J.; Ren, C. E.; Kwon, O.; Maleski, K.; Cho, S.-Y.; Anasori, B.; Kim, C.-K.; Choi, Y.-K.; Kim, J.; Gogotsi, Y.; Jung, H.-T. Metallic ${\rm Ti}_3{\rm C}_2{\rm T}_x$ MXene Gas Sensors with Ultrahigh Signal-to-Noise Ratio. ACS Nano 2018, 12, 986–993.
- (25) Pazniak, H.; Plugin, I. A.; Loes, M. J.; Inerbaev, T. M.; Burmistrov, I. N.; Gorshenkov, M.; Polcak, J.; Varezhnikov, A. S.; Sommer, M.; Kuznetsov, D. V.; Bruns, M.; Fedorov, F. S.; Vorobeva, N. S.; Sinitskii, A.; Sysoev, V. V. Partially Oxidized Ti₃C₂T_x MXenes for Fast and Selective Detection of Organic Vapors at Part-per-Million Concentrations. *ACS Appl. Nano Mater.* **2020**, *3*, 3195–3204.
- (26) Lee, E.; VahidMohammadi, A.; Prorok, B. C.; Yoon, Y. S.; Beidaghi, M.; Kim, D.-J. Room Temperature Gas Sensing of Two-Dimensional Titanium Carbide (MXene). ACS Appl. Mater. Interfaces 2017, 9, 37184–37190.
- (27) Choi, J.; Kim, Y.-J.; Cho, S.-Y.; Park, K.; Kang, H.; Kim, S. J.; Jung, H.-T. In Situ Formation of Multiple Schottky Barriers in a $\mathrm{Ti}_3\mathrm{C}_2$ MXene Film and its Application in Highly Sensitive Gas Sensors. *Adv. Funct. Mater.* **2020**, *30*, 2003998.
- (28) Tian, X.; Yao, L.; Cui, X.; Zhao, R.; Chen, T.; Xiao, X.; Wang, Y. A two-dimensional $\mathrm{Ti}_3\mathrm{C}_2\mathrm{T}_X$ MXene@ $\mathrm{TiO}_2/\mathrm{MoS}_2$ heterostructure with excellent selectivity for the room temperature detection of ammonia. *J. Mater. Chem. A* **2022**, *10*, 5505–5519.
- (29) Zhou, M.; Han, Y.; Yao, Y.; Xie, L.; Zhao, X.; Wang, J.; Zhu, Z. Fabrication of ${\rm Ti}_3{\rm C}_2{\rm T}_x/{\rm In}_2{\rm O}_3$ nanocomposites for enhanced ammonia sensing at room temperature. *Ceram. Int.* **2022**, 48, 6600–6607.
- (30) Jian, Y.; Qu, D.; Guo, L.; Zhu, Y.; Su, C.; Feng, H.; Zhang, G.; Zhang, J.; Wu, W.; Yao, M.-S. The prior rules of designing $Ti_3C_2T_x$ MXene-based gas sensors. *Front. Chem. Sci. Eng.* **2021**, *15*, 505–517.
- (31) Choi, J.; Chacon, B.; Park, H.; Hantanasirisakul, K.; Kim, T.; Shevchuk, K.; Lee, J.; Kang, H.; Cho, S. Y.; Kim, J.; Gogotsi, Y.; Kim, S. J.; Jung, H. T. N-p-Conductor Transition of Gas Sensing Behaviors in Mo₂CT_x MXene. *ACS Sens.* **2022**, *7*, 2225–2234.
- (32) Koh, H.-J.; Kim, S. J.; Maleski, K.; Cho, S.-Y.; Kim, Y.-J.; Ahn, C. W.; Gogotsi, Y.; Jung, H.-T. Enhanced Selectivity of MXene Gas Sensors through Metal Ion Intercalation: In Situ X-ray Diffraction Study. ACS Sens. 2019, 4, 1365–1372.
- (33) Hart, J. L.; Hantanasirisakul, K.; Lang, A. C.; Anasori, B.; Pinto, D.; Pivak, Y.; van Omme, J. T.; May, S. J.; Gogotsi, Y.; Taheri, M. L. Control of MXenes' electronic properties through termination and intercalation. *Nat. Commun.* **2019**, *10*, 522.
- (34) Muckley, E. S.; Naguib, M.; Wang, H. W.; Vlcek, L.; Osti, N. C.; Sacci, R. L.; Sang, X.; Unocic, R. R.; Xie, Y.; Tyagi, M.; Mamontov, E.; Page, K. L.; Kent, P. R. C.; Nanda, J.; Ivanov, I. N. Multimodality of Structural, Electrical, and Gravimetric Responses of Intercalated MXenes to Water. ACS Nano 2017, 11, 11118–11126.
- (35) Kim, S.; Lee, J.; Doo, S.; Kang, Y. C.; Koo, C. M.; Kim, S. J. Metal-Ion-Intercalated MXene Nanosheet Films for NH₃ Gas Detection. *ACS Appl. Nano Mater.* **2021**, *4*, 14249–14257.
- (36) Lee, J.; Kang, Y. C.; Koo, C. M.; Kim, S. J. $\text{Ti}_3\text{C}_2\text{T}_x$ MXene Nanolaminates with Ionic Additives for Enhanced Gas-Sensing Performance. *ACS Appl. Nano Mater.* **2022**, *5*, 11997–12005.
- (37) Zhang, Y.; Jiang, Y.; Duan, Z.; Huang, Q.; Wu, Y.; Liu, B.; Zhao, Q.; Wang, S.; Yuan, Z.; Tai, H. Highly sensitive and selective NO₂ sensor of alkalized V₂CT_x MXene driven by interlayer swelling. *Sens. Actuators, B* **2021**, 344, 130150.

- (38) Hantanasirisakul, K.; Gogotsi, Y. Electronic and Optical Properties of 2D Transition Metal Carbides and Nitrides (MXenes). *Adv. Mater.* **2018**, *30*, 1804779.
- (39) Wu, M.; An, Y.; Yang, R.; Tao, Z.; Xia, Q.; Hu, Q.; Li, M.; Chen, K.; Zhang, Z.; Huang, Q.; Ma, S.-H.; Zhou, A. V_2CT_x and $Ti_3C_2T_x$ MXenes Nanosheets for Gas Sensing. *ACS Appl. Nano Mater.* **2021**, *4*, 6257–6268.
- (40) Yamazoe, N.; Shimanoe, K. Fundamentals of semiconductor gas sensors. In *Semiconductor Gas Sensors*; Elsevier, 2020, pp. 3–38.
- (41) Zhang, H.-F.; Xuan, J.-Y.; Zhang, Q.; Sun, M.-L.; Jia, F.-C.; Wang, X.-M.; Yin, G.-C.; Lu, S.-Y. Strategies and challenges for enhancing performance of MXene-based gas sensors: a review. *Rare Met.* **2022**, *41*, 3976–3999.
- (42) Rathi, K.; Arkoti, N. K.; Pal, K. Fabrication of Delaminated 2D Metal Carbide MXenes (Nb₂CT_x) by CTAB-based NO₂ Gas Sensor with Enhanced Stability. *Adv. Mater. Interfaces* **2022**, *9*, 2200415.
- (43) An, H.; Habib, T.; Shah, S.; Gao, H.; Patel, A.; Echols, I.; Zhao, X.; Radovic, M.; Green, M. J.; Lutkenhaus, J. L. Water Sorption in MXene/Polyelectrolyte Multilayers for Ultrafast Humidity Sensing. ACS Appl. Nano Mater. 2019, 2, 948–955.
- (44) Mathis, T. S.; Maleski, K.; Goad, A.; Sarycheva, A.; Anayee, M.; Foucher, A. C.; Hantanasirisakul, K.; Shuck, C. E.; Stach, E. A.; Gogotsi, Y. Modified MAX Phase Synthesis for Environmentally Stable and Highly Conductive Ti₃C₂ MXene. *ACS Nano* **2021**, *15*, 6420–6429.
- (45) Shekhirev, M.; Busa, J.; Shuck, C. E.; Torres, A.; Bagheri, S.; Sinitskii, A.; Gogotsi, Y. Ultralarge Flakes of Ti₃C₂T_x MXene via Soft Delamination. *ACS Nano* **2022**, *16*, 13695–13703.
- (46) Alhabeb, M.; Maleski, K.; Anasori, B.; Lelyukh, P.; Clark, L.; Sin, S.; Gogotsi, Y. Guidelines for Synthesis and Processing of Two-Dimensional Titanium Carbide (Ti₃C₂T_x MXene). *Chem. Mater.* **2017**, *29*, 7633–7644.
- (47) Bagheri, S.; Lipatov, A.; Vorobeva, N. S.; Sinitskii, A. Interlayer Incorporation of A-Elements into MXenes Via Selective Etching of A' from $M_{n+1}A'_{1-x}A''_{x}C_{n}$ MAX Phases. ACS Nano **2023**, 17, 18747–18757.
- (48) Vorobeva, N. S.; Bagheri, S.; Torres, A.; Sinitskii, A. Negative photoresponse in Ti₃C₂T_x MXene monolayers. *Nanophotonics* **2022**, *11*, 3953–3960.
- (49) Loes, M. J.; Bagheri, S.; Vorobeva, N. S.; Abourahma, J.; Sinitskii, A. Synergistic Effect of TiS_3 and $Ti_3C_2T_x$ MXene for Temperature-Tunable p-/n-Type Gas Sensing. ACS Appl. Nano Mater. **2023**, *6*, 9226–9235.
- (50) Lipatov, A.; Lu, H.; Alhabeb, M.; Anasori, B.; Gruverman, A.; Gogotsi, Y.; Sinitskii, A. Elastic properties of 2D Ti₃C₂T_x MXene monolayers and bilayers. *Sci. Adv.* **2018**, *4*, No. eaat0491.
- (51) Ghidiu, M.; Lukatskaya, M. R.; Zhao, M.-Q.; Gogotsi, Y.; Barsoum, M. W. Conductive two-dimensional titanium carbide 'clay' with high volumetric capacitance. *Nature* **2014**, *516*, 78–81.
- (52) Wang, X.; Shen, X.; Gao, Y.; Wang, Z.; Yu, R.; Chen, L. Atomic-Scale Recognition of Surface Structure and Intercalation Mechanism of Ti₃C₂X. *J. Am. Chem. Soc.* **2015**, *137*, 2715–2721.
- (53) Hantanasirisakul, K.; Zhao, M.-Q.; Urbankowski, P.; Halim, J.; Anasori, B.; Kota, S.; Ren, C. E.; Barsoum, M. W.; Gogotsi, Y. Fabrication of ${\rm Ti}_3{\rm C}_2{\rm T}_x$ MXene Transparent Thin Films with Tunable Optoelectronic Properties. *Adv. Electron. Mater.* **2016**, *2*, 1600050.
- (54) Wu, M.; He, M.; Hu, Q.; Wu, Q.; Sun, G.; Xie, L.; Zhang, Z.; Zhu, Z.; Zhou, A. $\mathrm{Ti}_3\mathrm{C}_2$ MXene-Based Sensors with High Selectivity for NH $_3$ Detection at Room Temperature. *ACS Sens.* **2019**, *4*, 2763–2770.
- (55) Sajjad Hajian, P. K.; Moshayedi, M.; Maddipatla, D.; Narakathu, B. B.; Turkani, V. S.; Bazuin, B. J.; Pourfath, M.; Atashbar, M. Z. Impact of Different Ratios of Fluorine, Oxygen, and Hydroxyl Surface Terminations on ${\rm Ti}_3{\rm C}_2{\rm T}_{\rm x}$ MXene as Ammonia Sensor: A First-Principles Study. In 2018 IEEE Sensors; IEEE, 2018, pp. 1–4.
- (56) Late, D. J.; Huang, Y.-K.; Liu, B.; Acharya, J.; Shirodkar, S. N.; Luo, J.; Yan, A.; Charles, D.; Waghmare, U. V.; Dravid, V. P.; Rao, C.

- N. R. Sensing Behavior of Atomically Thin-Layered MoS₂ Transistors. *ACS Nano* **2013**, *7*, 4879–4891.
- (57) Barsoum, M. W.; Gogotsi, Y. Removing roadblocks and opening new opportunities for MXenes. *Ceram. Int.* **2023**, *49*, 24112–24122
- (58) Tang, J.; Wan, H.; Chang, L.; Hu, B.; Cui, S.; Chen, Y.; Chen, W.; Hao, J.; Tang, H.; Wang, X.; et al. Tunable Infrared Sensing Properties of MXenes Enabled by Intercalants. *Adv. Opt. Mater.* **2022**, 10, 2200623.
- (59) Chen, W. Y.; Lai, S.-N.; Yen, C.-C.; Jiang, X.; Peroulis, D.; Stanciu, L. A. Surface Functionalization of ${\rm Ti}_3{\rm C}_2{\rm T}_x$ MXene with Highly Reliable Superhydrophobic Protection for Volatile Organic Compounds Sensing. *ACS Nano* **2020**, *14*, 11490–11501.
- (60) Zhou, Y.; Jiang, Y.; Xie, T.; Tai, H.; Xie, G. A novel sensing mechanism for resistive gas sensors based on layered reduced graphene oxide thin films at room temperature. *Sens. Actuators, B* **2014**, 203, 135–142.
- (61) Lipatov, A.; Varezhnikov, A.; Wilson, P.; Sysoev, V.; Kolmakov, A.; Sinitskii, A. Highly selective gas sensor arrays based on thermally reduced graphene oxide. *Nanoscale* **2013**, *5*, 5426–5434.
- (62) Lipatov, A.; Guinel, M. J.-F.; Muratov, D. S.; Vanyushin, V. O.; Wilson, P. M.; Kolmakov, A.; Sinitskii, A. Low-temperature thermal reduction of graphene oxide: In situ correlative structural, thermal desorption, and electrical transport measurements. *Appl. Phys. Lett.* **2018**, *112*, 053103.
- (63) Shekhirev, M.; Lipatov, A.; Torres, A.; Vorobeva, N. S.; Harkleroad, A.; Lashkov, A.; Sysoev, V.; Sinitskii, A. Highly Selective Gas Sensors Based on Graphene Nanoribbons Grown by Chemical Vapor Deposition. ACS Appl. Mater. Interfaces 2020, 12, 7392–7402.